SHORT COMMUNICATION • **OPEN ACCESS**

Multi-taper-based automatic correction of non-anechoic antenna measurements

OPEN ACCESS
IOP Publishing | Bureau International des Poids et Mesures
Metrologia
Metrologia **61** (2024) 012101 (8pp)
https://doi.org/10.1088/1681-7575/ad10bd

Short Communication

Multi-taper-based automatic correction of non-anechoic antenna measurements

Mariusz Dzwonkowski[1,2], **Vorya Waladi**[1] **and Adrian Bekasiewicz**[1,*]

[1] Faculty of Electronics, Telecommunications and Informatics, Gdansk University of Technology, Gdansk, Poland
[2] Department of Radiology Informatics and Statistics, Faculty of Health Sciences, Medical University of Gdansk, Gdansk, Poland

E-mail: bekasiewicz@ru.is

Received 3 October 2023, revised 8 November 2023
Accepted for publication 29 November 2023
Published 7 December 2023

Abstract

Prototype measurements belong to the key steps in the development of antenna structures. Although accurate validation of their far-field performance can be realized in dedicated facilities, such as anechoic chambers, the high cost of their construction and maintenance might not be justified if the main goal of measurements is to support teaching or low-budget research. Instead, they can be performed in non-anechoic conditions and then refined using appropriate correction algorithms. Unfortunately, the existing post-processing methods suffer from multiple challenges that include manual setup of parameters as well as validation of performance in idealized conditions. In this communication, a multi-taper-based framework for correction of antenna characteristics obtained in non-anechoic environments has been proposed. The algorithm augments one-shot measurements of the structure under test in order to extract the line-of-sight responses while attenuating the interferences pertinent to multi-path propagation and noise from external sources of radiation. The performance of the proposed correction routine has been demonstrated in two test sites using a geometrically small Vivaldi radiator and validated against state-of-the-art techniques from the literature. The uncertainty budget for the measurements performed using the approach amounts to 0.26 dB, which is low given challenging propagation conditions considered for experiments.

Keywords: anechoic chamber, antenna measurement, auto-calibration, non-anechoic measurements, radiation pattern, multi-taper method, internet things

1. Introduction

Experimental validation of prototypes is an inherent step in the development of novel antenna geometries. It is normally performed in professional, dedicated laboratories that include anechoic chambers (ACs), compact-range, near-field, or open-test sites [1–8]. Despite high accuracy—resulting from strict control of the propagation environment—high construction cost of the mentioned facilities might be unjustified from the perspective of applications such as training of students, or budget-tight research. From this perspective, neglecting the control of radiation environment in favor of installing the equipment at sites deemed unsuitable for the validation of antenna far-field properties might substantially reduce measurement-related expenses [9]. Example locations include office cubicles, hallways, courtyards, or parks [9–11]. Unfortunately, the responses directly obtained in such

* Author to whom any correspondence should be addressed.

non-anechoic conditions are useless for rendering meaningful conclusions on the far-field performance of the antenna under test (AUT) [9–12].

The problem concerning insufficient fidelity of non-anechoic measurements can be mitigated using appropriate post-processing techniques. Popular methods are based on the concepts of: (i) signal decomposition and (ii) characterization of the propagation environment [9–31]. The first group involves extracting the useful part of the response—pertinent to line-of-sight transmission between the reference antenna (RA) and AUT—using time-, or frequency-domain methods [9–20]. The former exploits window functions centered around the signal pulse pertinent to direct transmission [9–14]. The frequency-based routines focus on approximating the relevant fraction of the response using truncated compositions of basis functions. The latter are in the form of, e.g. complex exponentials or spherical-wave coefficients [15–23]. Depending on the implementation, the correction process might involve the analysis of either single-, or multi-point data [19, 22]. The second class of methods is oriented towards extracting the effects of the propagation environment on the RA-AUT transmission. This is predominantly realized based on a series of independent measurements performed in the laboratory [12, 20, 24]. Practical approaches to the problem involve analysis of the AUT in multiple locations within the test-site [24], extraction of the noise floor in the environment [12], or estimation of the equivalent currents on a hull that encloses the radiator [28].

The above-mentioned methods suffer from multiple challenges that make them of limited use for measurements in uncontrolled environments. These include cognition-based (i.e. experience-driven) setup of correction parameters or validation of performance in conditions that represent a much less demanding environment compared to standard office rooms (e.g. ACs, or semi-ACs with installed reflected surfaces) [15–20, 32]. Furthermore, in the literature, the post-processing parameters are fine-tuned to the given test conditions, which hinders transferring the setup between test sites [18, 20, 24]. From this perspective, the problem pertinent to correcting antenna measurements performed in non-anechoic environments remains open.

In this communication, a framework for automatic correction of measurements performed in uncontrolled environments based on multi-taper functions has been proposed. The approach involves analysis of the RA-AUT impulse response using a series of discrete prolate spheroidal functions so as to augment the relevant part of the signal while attenuating the noise (in the form of electromagnetic radiation from external systems and/or multi-path interferences). Due to multi-modal character of the functional landscape, the post-processing results are obtained as a convex combination of responses refined using locally optimal multi-taper-based functions. The performance of the algorithm has been demonstrated based on a total of 20 experiments performed at two non-anechoic test sites. The tests involved measurements of far-field performance characteristics (radiation patterns) of a geometrically small Vivaldi antenna at a total of 10 unique frequencies. Evaluation of the method in terms of uncertainty budget yields 0.26 dB, which is low given the challenging propagation conditions. From the standpoint of radiology, practical applications of the considered antenna structure might include incorporation as a part of the microwave imaging system for breast cancer detection [33–35]. A comparison of the method against state-of-the-art techniques from the literature has also been provided.

2. Methodology

In this section, the multi-taper-based correction procedure is discussed. In order to make the work self-consistent, we provide a formulation of the problem pertinent to the refinement of non-anechoic measurements. Next, the correction procedure that involves transformation of the measurements as well as construction and optimization of the multi-taper kernel functions is explained. The section is summarized by a discussion of the proposed algorithm. The numerical results are provided in section 3, whereas benchmarks of the method and discussions are provided in section 4.

2.1. Problem formulation

Let $\boldsymbol{R}_u(\boldsymbol{\omega}, \boldsymbol{\theta})$ be the family of uncorrected S_{21} responses of the RA-AUT system [36]. Here, $\boldsymbol{\omega} = [\omega_1 \ \ldots \ \omega_k \ \ldots \ \omega_K]^T$ is the frequency sweep ($k = 1, \ldots, K$) around $f_0 = (\omega_K - \omega_1)/2$, with $B = \omega_K - \omega_1$ being the bandwidth around f_0, and $\boldsymbol{\theta} = [\theta_1 \ \ldots \ \theta_a \ \ldots \ \theta_A]^T$ the angle of AUT rotation w.r.t. RA. The response $\boldsymbol{R}_u(\boldsymbol{\omega}, \boldsymbol{\theta})$ is distorted by multi-path interferences and electromagnetic noise (i.e. from external systems that share the same frequency spectrum) which makes it of limited use for evaluating the real-world AUT performance. Next, let $\boldsymbol{R}_c^* = \boldsymbol{R}_c^*(f_0, \boldsymbol{\theta})$ be the refined response of the radiator (as a function of $\boldsymbol{\theta}$ angle) at the frequency of interest. The proposed post-processing involves spectral analysis of $\boldsymbol{R}_u(\boldsymbol{\omega}, \boldsymbol{\theta})$ using a multi-taper approach in order to obtain $\boldsymbol{R}_c^*(f_0, \boldsymbol{\theta})$, which is an approximation of the measurements conducted in a controlled setting, such as an anechoic chamber [1, 37].

2.2. Multi-taper-based response correction

A multi-taper approach enables spectral analysis of the signal. Compared to conventional Fourier-based methods, it maintains a trade-off between the frequency resolution and variance of the corrected responses [38–40]. The method generates a set of orthogonal taper functions—also referred to as discrete prolate spheroidal sequences (DPSSs)—that enable constructing low-bias, statistically consistent estimators capable of reducing spectral leakage of the data [38–42]. The multi-taper-based correction of the time series responses extracted from $\boldsymbol{R}_u(\boldsymbol{\omega}, \boldsymbol{\theta})$ is as follows.

Let $\boldsymbol{T}_u = \boldsymbol{T}_u(\boldsymbol{t}, \theta_a) = F^{-1}(\boldsymbol{R}_u, N)$ be the time-domain response at θ_a RA-AUT angle extracted from $\boldsymbol{R}_u = \boldsymbol{R}_u(\boldsymbol{\omega}, \theta_a)$ using an inverse Fourier transform (denoted as $F^{-1}(\cdot)$) with $N = 2^{\lceil \log_2 K \rceil + 3}$ ($\lceil \cdot \rceil$ is round-up to integer) [43]. The time sweep is $\boldsymbol{t} = [t_1, \ldots, t_N]^T = \partial t \cdot \boldsymbol{M}$, where $\partial t = (\omega_K - \omega_1)^{-1} \cdot (K-1)/(N-1)$ and $\boldsymbol{M} = [-N/2, \ldots, N/2-2, N/2-1]^T$, respectively. Then, let $\boldsymbol{T}_s = \boldsymbol{T}_u(\boldsymbol{t}_s, \theta_a)$ be the ith segment of

$\boldsymbol{T}_u$, such that $\boldsymbol{t}_s = \partial t{\cdot}\boldsymbol{M}_s$ and $\boldsymbol{M}_s = \boldsymbol{M}_s(i) = [-N/2+(i-1){\cdot}s, \ldots, -N/2+(i-1){\cdot}s + n-1]^T$. Here, $i = 1, 2, \ldots, \lfloor (N-n+s)/s \rfloor$ ($\lfloor\cdot\rfloor$ is round-down to integer), where $n = 1, 2, \ldots, N-1$ and $s = 1, 2, \ldots, n$ refer to the segment and step lengths, respectively (both defined in points). Note that $n = 1$ (and thus $s = 1$) will produce N segments of $\boldsymbol{T}_u$, each being of unit length (i.e. a single discrete time-instance), while for $n = N-1$ there will be $\lfloor (1+s)/s \rfloor$ segments of $N-1$ points in length (i.e. for $s = 1$ yielding $N-2$ points of overlap between consecutive $\boldsymbol{T}_u$ fractions, or a single non-overlapping segment for $s \neq 1$). Additionally, for $s = n$ there is no overlap between the subsequent $\boldsymbol{T}_u$ segments. In practice, overlapping of segments results in temporal interpolation of data that could increase the precision of spectral events identification (here, separation of the noise from the relevant part of the RA-AUT transmission) [38]. Here, $1 \leqslant s \leqslant n \leqslant N/2$ is assumed to ensure a reasonable $\boldsymbol{T}_u$ segmentation.

To perform multiple tapering of segments from $\boldsymbol{T}_u$, one has to define appropriate DPSS kernels. The problem corresponds to finding the n-point finite energy sequences that maximize the spectral concentration ratio for the selected $2W$ bandwidth, where $W < 0.5\partial t^{-1}$. The sequences and their concentrations can be represented using a composition of eigenvectors and their corresponding eigenvalues (bounded by 1) of the n-by-n self-adjoint positive semidefinite operator [44–47]. Considering the ith segment of $\boldsymbol{T}_u$, the process of finding all DPSS kernels $\boldsymbol{T}_\kappa(\boldsymbol{t}_s, w)$ can be formulated as follows:

$$\sum_{\rho=0}^{n-1} \frac{\sin\left(2\pi\left(\gamma-\rho\right)\cdot W\right)}{\pi\left(\gamma-\rho\right)} \cdot \boldsymbol{T}_\kappa\left(\boldsymbol{t}_s\left(\rho\right), w\right) = \lambda_w \cdot \boldsymbol{T}_\kappa\left(\boldsymbol{t}_s\left(\gamma\right), w\right) \tag{1}$$

where $w = 0, 1, \ldots, n-1$ denotes the order of the identified sequence, $\gamma = 0, 1, \ldots, n-1$, whereas λ_w is the eigenvalue of the corresponding eigenvector $\boldsymbol{T}_\kappa(\boldsymbol{t}_s, w)$ of order w. Note that the $2W$ bandwidth defines the spectral resolution of the multitaper method, i.e. the main lobe width in the spectral estimate, which controls the minimum distance between peaks that can be resolved [38, 42]. The optimal number of DPSS tapers is given as $w_{\text{opt}} = \lfloor 2t_{HB} \rfloor - 1$, where $t_{HB} = n{\cdot}\partial t{\cdot}W < n/2$ is a time-half-bandwidth product [38, 42]. The example DPSS sequences—with normalized amplitude and $\partial t = 1$ ns (for visualization)—obtained using (1) are shown in figure 1(a).

Upon identification of kernels, the post-processing of non-anechoic measurements is performed as follows. Each predetermined segment of the data time series is modified using w_{opt} tapers. Then, the n-point Fourier transforms of individual events are calculated, and their convex combination (weighted using the eigenvalues λ_w) is calculated to get the frequency-domain response for each segment. The process for the ith segment $\boldsymbol{T}_s$ can be depicted as:

$$\boldsymbol{R}_{cs}\left(\boldsymbol{\Omega}_s, \theta_a\right) = \sum_{w=0}^{w_{\text{opt}}-1} F\left(\boldsymbol{T}_s \circ \boldsymbol{T}_\kappa\left(\boldsymbol{t}_s, w\right), n\right) \cdot \frac{\lambda_w}{\sum_{w'=0}^{w_{\text{opt}}-1} \lambda_{w'}} \tag{2}$$

where the symbol $\circ$ denotes the component-wise multiplication, $\boldsymbol{R}_{cs}(\boldsymbol{\Omega}_s, \theta_a)$ is the frequency-domain response for the ith segment $\boldsymbol{T}_s$, and $\boldsymbol{\Omega}_s = \partial\omega{\cdot}\boldsymbol{M}_s$ for $\partial\omega = (t_N - t_1)^{-1}$. Concatenating the frequency-domain responses for every segment and applying arithmetic mean to the overlapping points (when $s < n$), will yield the frequency-domain response $\boldsymbol{R}_c(\boldsymbol{\Omega}, \theta_a)$, such that $\boldsymbol{\Omega} = \partial\omega{\cdot}\boldsymbol{M}_\omega$, where $\boldsymbol{M}_\omega = [-N/2, \ldots, -N/2+(\lfloor (N-n+s)/s \rfloor - 1){\cdot}s + n-1]^T$. The corrected non-anechoic response of the RA-AUT system $R_c(f_0, \theta_a)$ is extracted at $f_0 \in \boldsymbol{\Omega}$ (note that $\boldsymbol{\omega} \in \boldsymbol{\Omega}$) and θ_a angle. To find the $\boldsymbol{R}_c(f_0, \boldsymbol{\theta})$, the above-outlined procedure is executed for all θ_a angles.

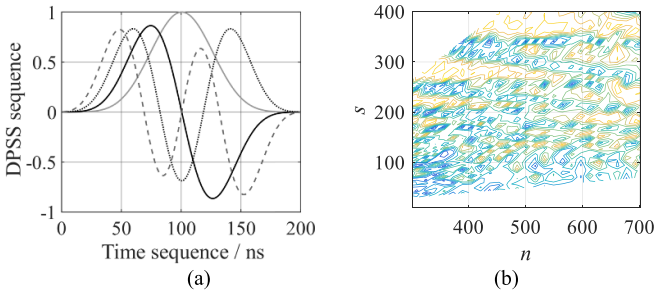

Figure 1. DPSS correction: (a) normalized kernels of order $w = 0$ (gray), as well as (black) $w = 1$ (—), $w = 2$ (···), and $w = 3$ (- -) for $n = 200$ and $t_{\text{HB}} = 5$), and (b) visualization of a multimodal functional landscape obtained using (3), where warmer/darker colors represent hills/valleys. Note that s and n are (unit-less) sample indices.

2.3. Identification of optimal DPSS parameters

The DPSS-based correction performance heavily depends on the determination of appropriate segment lengths n and steps s, whereas the effects of W and t_{HB} on the behavior of kernel functions are less pronounced (here, $t_{\text{HB}} = 4$ is used). The optimal number of segments and steps required to refine the measurements performed at the given frequency of interest are identified using the scalar objective function of the form:

$$U(\boldsymbol{x}) = \sum\left(\boldsymbol{R}_c(\boldsymbol{x}) - \alpha\boldsymbol{R}_f(f_0, \boldsymbol{\theta})\right) \tag{3}$$

where $\boldsymbol{x} = [x_1\ x_2]^T = [n\ s]^T$ is the vector of setup parameters, $\boldsymbol{R}_c(\boldsymbol{x})$ is the corrected $\boldsymbol{R}_c(f_0, \boldsymbol{\theta})$ response obtained using the DPSS kernels resulting from $\boldsymbol{x}$, and $\boldsymbol{R}_f = \boldsymbol{R}_f(f_0, \boldsymbol{\theta})$ is the reference performance figure (here radiation pattern) obtained from EM simulations. The multiplicative factor $\alpha = (\boldsymbol{R}_f{}^T\boldsymbol{R}_f)^{-1}\boldsymbol{R}_f{}^T\boldsymbol{R}_c(\boldsymbol{x})$ represents an analytical solution to the curve fitting problem that minimizes the discrepancy between $\boldsymbol{R}_c(\boldsymbol{x})$ and $\boldsymbol{R}_f$ through appropriate (single-value) scaling of the latter. The goal of scaling is to ensure that minimization of (3) is oriented towards identification of DPSS components that maintain the appropriate shape of $\boldsymbol{R}_c(\boldsymbol{x})$ rather than match its amplitude to the one resulting from simulations. In other words, it aids in rejecting the responses that do not resemble the expected antenna response. As shown in figure 1(b), the example DPSS-based functional landscape resulting from (3) is highly multimodal, which makes identification of optimum parameters difficult. Here, the problem is mitigated using the exhaustive search procedure where the objective function (3) is evaluated for a set of designs $\boldsymbol{X} = \{\boldsymbol{x}_p\}_{1 \leqslant p \leqslant P}$. Next, the

domination-based ranking is performed in order to identify a set of $\boldsymbol{X}_{\text{opt}} \subset \boldsymbol{X}$ designs that correspond to local minima. The corrected responses $\boldsymbol{R}_c(\boldsymbol{X}_{\text{opt}})$ are then used to extract the final result $\boldsymbol{R}_c^{\,*}$. The latter is obtained as an average of solutions $\boldsymbol{R}_c(\boldsymbol{x}_\beta)$, $\beta = 1, 2, \ldots$, and $\boldsymbol{x}_\beta \in \boldsymbol{X}_{\text{opt}}$, that represent the σ-quantile of all locally optimal responses (here, $\sigma = 0.1$).

2.4. Summary of the approach

The presented framework for correction of non-anechoic measurements using a multi-taper-based approach can be summarized as follows:

1. Set f_0, K, B, N, and measure $\boldsymbol{R}_u(\boldsymbol{\omega}, \boldsymbol{\theta})$ data;
2. Set t_{HB} and define a set of $\boldsymbol{X} = \{\boldsymbol{x}_p\}_{1 \leqslant p \leqslant P}$ DPSS design parameters for exhaustive search; set $p = 1$;
3. Identify DPSS tapers from (1) using $\boldsymbol{x} = \boldsymbol{x}_p$ and setup (2) for all segments of the time series;
4. Determine $\boldsymbol{R}_c(\boldsymbol{\Omega}, \theta_a)$ and extract the ath element $R_c(f_0, \theta_a)$ of the $\boldsymbol{R}_c(f_0, \boldsymbol{\theta})$ vector;
5. If $a = A$, go to Step 6; otherwise, set $a = a + 1$ and go to Step 4.
6. Evaluate the function $U(\boldsymbol{x}_p)$ and store the $\boldsymbol{R}_c(\boldsymbol{x}_p)$;
7. If $p < P$, set $p = p + 1$ and go to Step 3; otherwise, go to Step 8;
8. Rank the obtained $U(\boldsymbol{X})$ responses to identify $\boldsymbol{R}_c(\boldsymbol{X}_{\text{opt}})$, and extract $\boldsymbol{R}_c^{\,*}$ as the average of $\boldsymbol{R}_c(\boldsymbol{x}_\beta)$, $\boldsymbol{x}_\beta \in \boldsymbol{X}_{\text{opt}}$, that correspond to σ-quantile locally optimal solutions; END.

The resulting vector $\boldsymbol{R}_c^{\,*}(f_0, \boldsymbol{\theta})$ represents the corrected AUT responses. Note that the final post-processing step can involve normalization of $\boldsymbol{R}_c^{\,*}$ followed by its conversion to decibels. It should be emphasized that the presented approach executes correction based on one-shot measurements and that the DPSS taper parameters are adjusted in an automated manner (i.e. without engineering inference). To the best knowledge of the authors, this is the first implementation of the multi-taper approach for the correction of non-anechoic antenna measurements.

3. Correction results

The proposed correction framework has been validated based on a series of 20 experiments performed in two non-anechoic test-sites (i.e. office rooms) that are not tailored to far-field experiments in any way except for the installation of the mobile positioning towers, the vector network analyzer (VNA), and the required cables and adapters [9]. The dimensions of the considered sites are 8.4 m^3 × 4.5 m^3 × 3.1 m^3 for room A and 5.5 m^3 × 4.5 m^3 × 3.1 m^3 for room B, respectively (cf figure 2). The AUT considered for the experiments is a spline-parameterized antipodal Vivaldi antenna of figure 3 [9, 48]. Owing to its far-field properties and broadband operation, the structure could be utilized as a part of the microwave-based imaging system dedicated to evaluation of living tissues, e.g. for the purpose of breast cancer detection [33–35]. Note that, for the considered experiments, the structure is also used

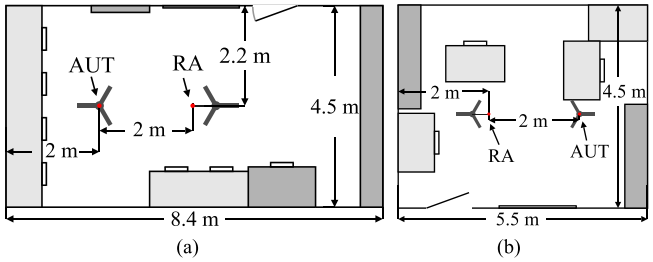

Figure 2. Non-anechoic test-sites considered for experiments with highlight on location of the positioning towers: (a) room A and (b) room B. Light- and dark-shade colors represent short and tall furniture, respectively. The antennas mounted on towers are denoted using red dots.

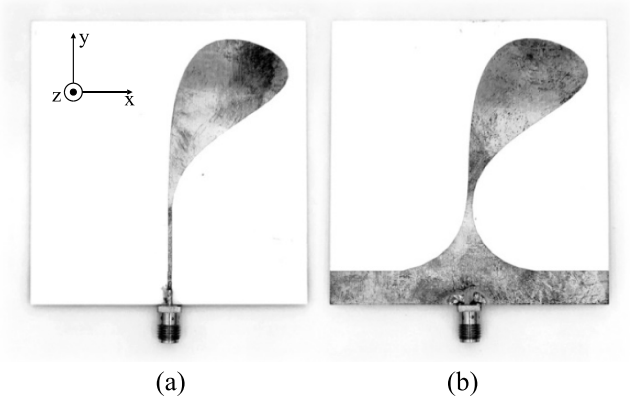

Figure 3. A photograph of the spline-parameterized antipodal Vivaldi antenna considered for experiments: (a) top and (b) bottom views.

as the RA. The test setup is as follows. The angular resolution is set to 5°, the number of frequency points around f_0 and the bandwidth are set to $K = 201$ and $B = 1$ GHz [9]. For both experiments, the AUT responses have been measured in the yz-plane (cf figure 3) at the following frequencies of interest $f_0 \in \{3, 4, 5, 6, 7, 8, 9, 10, 11, 12\}$ GHz. The post-processing performance has been expressed in terms of the—decibel-based—root-mean-square error e_R calculated w.r.t. the measurement results obtained for the same structure in the anechoic chamber.

3.1. Case study—test site A

Our first case study encompasses the measurements performed at the site A. The post-processing, associated with the multi-taper method (see section 2), is executed independently at each f_0 frequency of interest. Upon data acquisition, an optimal setup of DPSS tapers is identified based on the exhaustive search procedure outlined in section 2.3. The candidate DPSS kernels have been defined according to the set of test designs $\boldsymbol{X}$. The lower- and upper-bounds for the latter are specified as: $\boldsymbol{l}_b = [101\ 0.1x_1]^T$ and $\boldsymbol{u}_b = [901\ 0.9x_1]^T$. It should be noted that the linear scaling of the second parameter ensures that $s < n$ (cf section 2.2). Its effects on the shape of the search space at the 4 GHz frequency are shown in figure 1(b). After evaluation,

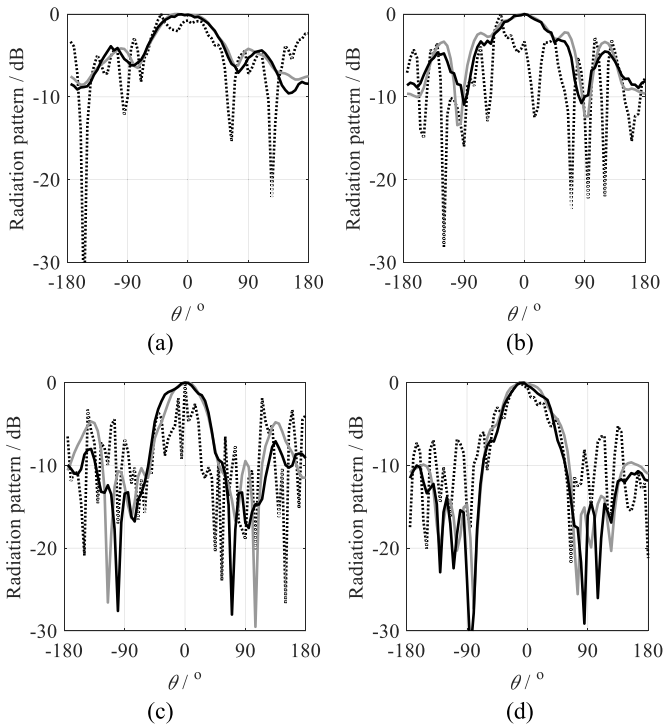

Figure 4. Test site A—AC-based patterns (gray) and the non-anechoic responses before (···), and after DPSS-based correction (—) at: (a) 4 GHz, (b) 5 GHz, (c) 6 GHz, and (d) 7 GHz frequencies.

Table 1. Test Site A: Correction Performance.

f_0/GHz	3	4	5	6	7	8	9	10	11	12
$e_R(\boldsymbol{R}_u)$/dB	–12.2	–19.8	–17.0	–11.5	–17.5	–18.3	–16.7	–16.1	–17.5	–13.2
$e_R(\boldsymbol{R}_c^*)$/dB	–21.9	–31.0	–22.1	–20.5	–25.2	–23.2	–22.8	–22.3	–22.6	–21.3
Δ/dB	9.7	11.2	5.1	9.0	7.7	4.9	6.1	6.2	5.1	8.1

the $\boldsymbol{R}_c(\boldsymbol{X})$ responses are ranked according to their corresponding $\boldsymbol{U}(\boldsymbol{X})$ values. The final solution is then identified as the average of $\boldsymbol{R}_c(\boldsymbol{x}_\beta)$ responses featuring the highest rank among the corrected measurements. Here, the number of considered designs amount to five which corresponds to the σ-quantile of the locally optimal solutions (with $\sigma = 0.1$). The procedure is repeated for all of the considered f_0 frequencies.

The antenna performance characteristics before and after correction are summarized in table 1. The refinement results indicate that the average improvement of the non-anechoic measurements fidelity due to the application of the proposed framework—expressed in terms of e_R—amounts to over 7.3 dB (i.e. decrease of the e_R factor from—16 dB to—23.3 dB) with maximum and minimum change of the non-anechoic response quality of 11.2 dB at 4 GHz and 4.9 dB at 8 GHz, respectively. Note that the difference between the responses fidelity before and after the correction process is expressed in terms of $\Delta = |e_R(\boldsymbol{R}_c^*(f_0, \boldsymbol{\theta}))—e_R(\boldsymbol{R}_u(f_0, \boldsymbol{\theta}))|$ dB. Figure 4 shows a comparison of the radiation pattern characteristics obtained for the antenna at the selected frequencies of interest before and after the post-processing. As already indicated by the results of table 1, the fidelity improvement of the real-world antenna performance evaluated in a non-anechoic environment due to post-processing is substantial.

3.2. Case study—test site B

For our second case study, the usefulness of the proposed correction framework has been demonstrated based on a total of ten experiments performed at the second test site. The latter (due to the smaller volume as well as the increased amount of more tightly packed furniture) represents a more challenging propagation environment compared to room A. The results summarized in table 2 indicate that the average improvement of the obtained non-anechoic responses due to the correction amounts to over 8.1 dB (i.e. decrease of the e_R error from—15.1 dB to—23.2 dB), with the maximum and minimum change of the response quality equal to 12.8 dB at 4 GHz and 4 dB at 12 GHz, respectively. A comparison of the radiation patterns obtained before and after the refinement is shown in figure 5. Similarly, as for the results obtained at the site A, the improvement in response fidelity is noticeable.

Table 2. Test Site B: Correction Performance.

f_0/GHz	3	4	5	6	7	8	9	10	11	12
$e_R(\boldsymbol{R}_u)$/dB	–12.9	–15.2	–10.9	–12.2	–16.1	–17.5	–17.1	–16.5	–15.1	–17.3
$e_R(\boldsymbol{R}_c^*)$/dB	–22.2	–28.0	–22.2	–19.0	–24.0	–25.4	–25.0	–22.8	–22.3	–21.3
Δ/dB	9.3	12.8	11.3	6.8	7.9	7.9	7.9	6.3	7.2	4

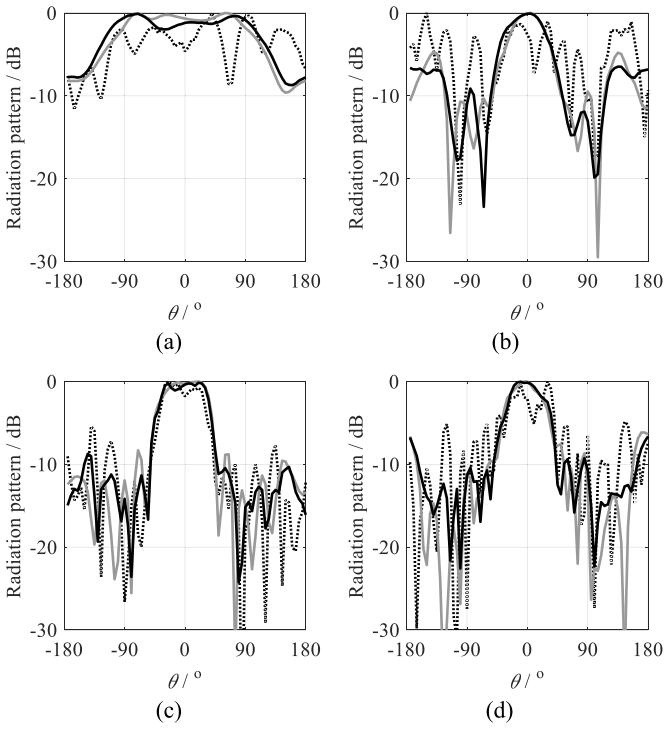

Figure 5. Test site B—AC-based patterns (gray) and the non-anechoic responses before (···), and after DPSS-based correction (—) at: (a) 3 GHz, (b) 6 GHz, (c) 10 GHz, and (d) 12 GHz frequencies.

4. Discussion and comparisons

The proposed correction framework has been subjected to a comparative analysis (in both test sites) against the state-of-the-art post-processing algorithms that involve time-domain analysis of the signal. The setup of benchmark methods includes the determination of intervals (pertinent to the relevant part of the RA-AUT transmission) based on: (i) manual estimation of the RA-AUT distance (with rectangular window function), (ii) cognition-based analysis of the impulse response (with Hann function), and (iii) determination of intervals using a composite window [12–14, 32]. To ensure an equitable comparison, the configuration parameters, i.e. f_0, *K, B, N* remain the same for all of the methods. The results presented in table 3 demonstrate that, for the considered test sites and the AUT at hand, the proposed multi-taper-based framework yields the most effective correction performance in terms of the averaged e_R factor. The improvement of the refined radiation patterns compared to the benchmark approaches ranges from 1.6 dB to 1.8 dB for site A and from 0.4 dB to 1 dB for site B, respectively. Furthermore, it should be noted that the average correction results obtained using the proposed framework are consistent across the test sites, whereas for the benchmark methods, the errors range from 0.6 dB to 1.2 dB, respectively. Another important remark is that, contrary to (i) and (ii), the presented approach does not rely on engineering insight. At the same time, compared to (iii)—where composite function parameters are based on a set of pre-defined threshold values—the exhaustive search of parameters implemented in the proposed algorithm ensures an increased number of degrees of freedom for tuning the kernel functions, which might result in improved flexibility in terms of the range of radiators and test-sites that can be supported.

Evaluation of the method in terms of uncertainty has also been considered. Due to challenging and time-consuming setup, the experiments have been performed only in the test site B and at a single frequency of interest, i.e. 4 GHz. The uncertainty budget has been estimated as follows [6]:

$$\delta = \sqrt{\sum_{p=1}^{P} {\delta_p}^2} \tag{4}$$

where each contributor δ_p, $p = 1, \ldots, P$ (here, $P = 5$) has been evaluated based on a series of measurements tailored to extract the factors such as: (i) dynamics of the environment (here understood as temporal changes of propagation conditions due to external factors)—δ_1, (ii) mutual alignment of the

Table 3. Benchmark of the Proposed Method.

	Correction method performance (average e_R)[a]			
Non-anechoic test site	(i)	(ii)	(iii)	This work
First	–21.7 dB	–21.5 dB	–21.7 dB	–23.3 dB
Second	–22.3 dB	–22.5 dB	–22.9 dB	–23.3 dB

[a] Averaged over the frequencies of interest.

RA-AUT system components—δ_2, (iii) VNA calibration—δ_3, (iv) repeatability of interconnections realized through microwave adapters—δ_4, and (v) cable bends—δ_5 [6]. It should be noted that uncertainty of the propagation environment is subject to (slight) variations of temperature, but also repeatability of angular alignment maintained by stepper motors in the rotary towers, noise introduced by the rotary adapters, and/or aliasing effects introduced in the course of the post-processing using the proposed algorithm. Consequently, the mentioned factors cannot be easily isolated to account for their individual contribution to (i) in the course of the post-processing. The extracted values of individual factors amount to 0.11 dB, 0.03 dB, 0.01 dB, 0.01 dB, and 0.23 dB—for (i)–(v), respectively. The resulting uncertainty budget derived from (4) is 0.26 dB, which indicates a high performance of the proposed correction approach. It is worth noting that, for (v), a relatively large variations are due to unfavorable testing conditions through measurements of the scattering parameters through a cable coiled around the 30 mm diameter cylinder (single turn), as well as upon its straightening (which is exaggerated compared to routine experiments).

5. Conclusion

In this work, a framework based on multi-tapered functions has been proposed for correcting the antenna measurements performed in non-anechoic environments. The approach involves augmenting the RA-AUT transmission obtained as a result of a series of one-shot measurements (each for a unique angular position of the RA-AUT system) using a series of spheroidal functions so as to separate the useful fraction of the signal from the interferences and noise. The performance of the algorithm has been demonstrated based on a series of 20 measurements of a geometrically small antipodal Vivaldi structure performed at two non-anechoic test sites. For the considered structure and experiments, the average improvement of the measured responses resulting from the application of the method amounts to around 8 dB w.r.t. uncorrected signals. The approach has been favorably compared against the state-of-the-art techniques from the literature that involve time-domain-based processing of the far-field responses. The uncertainty budget for correction using the proposed method amounts to 0.26 dB, which is low given the challenging experimental conditions provided by the considered non-anechoic measurement system.

Future work will focus on the enhancement of the proposed algorithm so as to enable automatic determination of all parameters that are relevant from the perspective of correction performance. Combination of the algorithm with alternative techniques oriented towards augmenting the amount of information that can be extracted from one-shot measurements will also be considered.

Acknowledgments

This work was supported in part by the National Science Centre of Poland Grant 2021/43/B/ST7/01856, National Centre for Research and Development Grant NOR/POLNOR/HAPADS/0049/2019-00, as well as Gdansk University of Technology (Excellence Initiative—Research University) Grant 16/2023/IDUB/IV.2/EUROPIUM.

ORCID iDs

Mariusz Dzwonkowski https://orcid.org/0000-0003-3580-7448
Adrian Bekasiewicz https://orcid.org/0000-0003-0244-541X

References

[1] Hemming L 2002 *Electromagnetic Anechoic Chambers: A Fundamental Design and Specification Guide* (IEEE Press)
[2] Knott E F *et al* 1993 *Radar Cross Section* 2nd edn (Artech House)
[3] Burnside W D *et al* 1999 An enhanced tapered chamber design *Ant. Meas. Tech. Assoc. Proc.* (*Monterey Bay, CA*)
[4] Li X, Chen L, Wang Z, Yang K and Miao J 2022 An ultra-wideband plane wave generator for 5G base station antenna measurement *Electronics* **12** 1824
[5] Zhang F, Zhang Y, Wang Z and Fan W 2023 Plane wave generator in non-anechoic radio environment *IEEE Antennas Wirel. Propag. Lett.* **22** 2896–900
[6] Kurokawa S, Hirose M and Komiyama K 2009 Measurement and uncertainty analysis of free-space antenna factors of a log-periodic antenna using time-domain techniques *IEEE Trans. Instrum. Meas.* **58** 1120–5
[7] Yaghjian A 1986 An overview of near-field antenna measurements *IEEE Trans. Antennas Propag.* **34** 30–45
[8] Kalashnikov V *et al* 2021 *Near Field Antenna Measurements: Calculations and Facility Design* (Springer)
[9] Olencki J, Waladi V, Bekasiewicz A and Leifsson L 2023 A low-cost system for far-field non-anechoic measurements of antenna performance figures *IEEE Access* **11** 39165–75
[10] Piasecki P and Strycharz J 2015 Measurement of an omnidirectional antenna pattern in an anechoic chamber and an office room with and without time domain signal processing *2015 Signal Processing Symp. (Spsympo)* (*Debe, Poland*) pp 1–4

[11] Clouston E N, Langsford P A and Evans S 1988 Measurement of anechoic chamber reflections by time-domain techniques *IEE Proc.* **135** 93–97

[12] de Sao Jose A N, Deniau V, Resende U C and Adriano R 2020 Improving antenna gain estimations in non-ideal test sites with auto-tunable filters *Measurement* **159** 107720

[13] Loredo S, Pino M R, Las-Heras F and Sarkar T K 2004 Echo identification and cancellation techniques for antenna measurement in non-anechoic test sites *IEEE Antennas Propag. Mag.* **46** 100–7

[14] Soltane A, Andrieu G, Perrin E, Decroze C and Reineix A 2020 Antenna radiation pattern measurement in a reverberating enclosure using the time-gating technique *IEEE Antennas Wirel. Propag. Lett.* **19** 183–7

[15] Fourestie B, Altman Z, Wiart J and Azoulay A 1999 On the use of the matrix-pencil method to correlate measurements at different test sites *IEEE Trans. Antennas Propag.* **47** 1569–73

[16] Du Z, Moon J I, Oh S-S, Koh J and Sarkar T K 2010 Generation of free space radiation patterns from non-anechoic measurements using Chebyshev polynomials *IEEE Trans. Antennas Propag.* **58** 2785–90

[17] Fiumara V, Fusco A, Iadarola G, Matta V and Pinto I M 2016 Free-space antenna pattern retrieval in nonideal reverberation chambers *IEEE Trans. Electromagn. Compat.* **58** 673–7

[18] Leon G, Loredo S, Zapatero S and Las-Heras F 2009 Radiation pattern retrieval in non-anechoic chambers using the matrix pencil algorithm *Prog. Electromagn. Res. Lett.* **9** 119–27

[19] Fourestie B and Altman Z 2001 Gabor schemes for analyzing antenna measurements *IEEE Trans. Antennas Propag.* **49** 1245–53

[20] Koh J, De A, Sarkar T K, Moon H, Zhao W and Salazar-Palma M 2012 Free space radiation pattern reconstruction from non-anechoic measurements using an impulse response of the environment *IEEE Trans. Antennas Propag.* **60** 821–31

[21] de Sao Jose A N *et al* 2017 Uncertainties minimization in open environment antenna gain estimations *IEEE Global EMC Conf.*

[22] Sierra-Castaner M, Gonzalez-Blanco P, Lopez Morales M J, Saccardi F and Foged L J 2015 Time and spatial filtering for echo reduction in antenna measurements *Antenna Measurement Techniques Association (AMTA)* (*Long Beach, USA*) pp 1–5

[23] Cano-Facila F J, Burgos S, Martín F and Sierra-Castaner M 2011 New reflection suppression method in antenna measurement systems based on diagnostic techniques *IEEE Trans. Antennas Propag.* **59** 941–9

[24] Froes S M, Corral P, Novo M S, Aljaro M and Lima A C C 2019 Antenna radiation pattern measurement in a nonanechoic chamber *IEEE Antennas Wirel. Propag. Lett.* **18** 383–6

[25] Schmidt C H and Eibert T F 2009 Near-field far-field transformation in echoic measurement environments employing scattering center representations *2009 3rd European Conf. on Antennas and Propagation* (*Berlin, Germany*) pp 3370–4

[26] Araque Quijano J L *et al* 2011 Source reconstruction in advanced processing of antenna measurements *Proc. 5th European Conf. on Antennas and Propagation (EUCAP)* (*Rome, Italy*) pp 3875–9

[27] Lopez Y A, Laviada J, Garcia-Gonzalez C and Las-Heras F 2012 Antenna characterization with multiple scatterers by means of equivalent currents and spherical wave expansion *2012 6th European Conf. on Antennas and Propagation (EUCAP)* (*Prague, Czech Republic*) pp 2551–4

[28] Knapp J, Kornprobst J and Eibert T F 2019 Equivalent source and pattern reconstruction from oversampled measurements in highly reflective environments *IET Microw. Antennas Propag.* **13** 2232–41

[29] Moon J-I, Oh S-S and Jung Y-B 2009 Echo-cancellation technique with recursive data in nonanechoic test sites *IEEE Antennas Wirel. Propag. Lett.* **8** 558–60

[30] Gonzalez-Blanco P and Sierra-Castaner M 2017 Analysis of time filtering techniques for echo reduction in antenna measurements *Int. J. Microw. Wirel. Technol.* **9** 1387–95

[31] Gifuni A, Ambrosanio M, Gradoni G, Grassini G, Smartt C and Perna S 2020 Measurement of the antenna impedance mismatch through the time domain mode of the vector network analyzers: an experimental procedure *Prog. Electromagn. Res.* B **87** 131–49

[32] Mroczka J 2013 The cognitive process in metrology *Measurement* **46** 2896–907

[33] Hagness S C, Taflove A and Bridges J E 1998 Two-dimensional FDTD analysis of a pulsed microwave confocal system for breast cancer detection: fixed-focus and antenna-array sensors *IEEE Trans. Biomed. Eng.* **45** 1470–9

[34] Woten A, Lusth J and El-Shenawee M 2007 Interpreting artificial neural networks for microwave detection of breast cancer *IEEE Microw. Wirel. Compon. Lett.* **17** 825–7

[35] Lu M, Xiao X, Pang Y, Liu G and Lu H 2022 Detection and localization of breast cancer using UWB microwave technology and CNN-LSTM framework *IEEE Trans. Microw. Theory Technol.* **70** 5085–94

[36] Balanis C A 2005 *Antenna Theory Analysis and Design* 3rd edn (Wiley)

[37] Cohen M X 2014 *Analyzing Neural Time Series Data: Theory and Practice* (MIT Press)

[38] Prerau M J, Brown R E, Bianchi M T, Ellenbogen J M and Purdon P L 2017 Sleep neurophysiological dynamics through the lens of multitaper spectral analysis *Physiology* **32** 60–92

[39] Bronez T 1992 On the performance advantage of multitaper spectral analysis *IEEE Trans. Signal Process.* **40** 2941–6

[40] Percival D B and Walden A T 1993 *Spectral Analysis for Physical Applications: Multitaper and Conventional Univariate Techniques* (Cambridge University Press)

[41] Thomson D J 1982 Spectrum estimation and harmonic analysis *Proc. IEEE* **70** 1055–96

[42] Babadi B and Brown E N 2014 A review of multitaper spectral analysis *IEEE Trans. Biomed. Eng.* **61** 1555–64

[43] Oppenheim A V and Schafer R W 2009 *Discrete-Time Signal Processing* 3rd edn (Prentice Hall)

[44] Slepian D 1978 Prolate spheroidal wave functions, Fourier analysis, and uncertainty—V: the discrete case *Bell Syst. Tech. J.* **57** 1371–430

[45] Hristopulos D T 2021 Discrete prolate spheroidal sequence *Encyclopedia of Mathematical Geosciences* (*Encyclopedia of Earth Sciences Series*) ed B S Daya Sagar *et al* (Springer)

[46] Riedel K S and Sidorenko A 1995 Minimum bias multiple taper spectral estimation *IEEE Trans. Signal Process.* **43** 188–95

[47] McCoy E J, Walden A T and Percival D B 1998 Multitaper spectral estimation of power law processes *IEEE Trans. Signal Process.* **46** 655–68

[48] Bai J, Shi S and Prather D W 2011 Modified compact antipodal Vivaldi antenna for 4–50-GHz UWB application *IEEE Trans. Microw. Theory Technol.* **59** 1051–7